

Accepted Manuscript

Radiation tolerant ceramics for nuclear waste immobilization: Structure and stability of cesium containing hollandite of the form $(\text{Ba,Cs})_{1.33}(\text{Zn,Ti})_8\text{O}_{16}$ and $(\text{Ba,Cs})_{1.33}(\text{Ga,Ti})_8\text{O}_{16}$

R. Grote, T. Hong, L. Shuller-Nickles, J. Amoroso, M. Tang, K. Brinkman

PII: S0022-3115(18)31540-X

DOI: <https://doi.org/10.1016/j.jnucmat.2019.03.005>

Reference: NUMA 51497

To appear in: *Journal of Nuclear Materials*

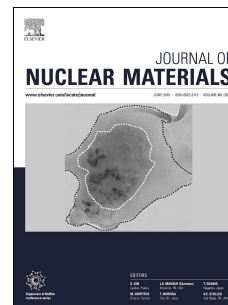
Received Date: 9 November 2018

Revised Date: 2 March 2019

Accepted Date: 4 March 2019

Please cite this article as: R. Grote, T. Hong, L. Shuller-Nickles, J. Amoroso, M. Tang, K. Brinkman, Radiation tolerant ceramics for nuclear waste immobilization: Structure and stability of cesium containing hollandite of the form $(\text{Ba,Cs})_{1.33}(\text{Zn,Ti})_8\text{O}_{16}$ and $(\text{Ba,Cs})_{1.33}(\text{Ga,Ti})_8\text{O}_{16}$, *Journal of Nuclear Materials* (2019), doi: <https://doi.org/10.1016/j.jnucmat.2019.03.005>.

This is a PDF file of an unedited manuscript that has been accepted for publication. As a service to our customers we are providing this early version of the manuscript. The manuscript will undergo copyediting, typesetting, and review of the resulting proof before it is published in its final form. Please note that during the production process errors may be discovered which could affect the content, and all legal disclaimers that apply to the journal pertain.



Radiation Tolerant Ceramics for Nuclear Waste Immobilization: Structure and Stability of Cesium Containing Hollandite of the form $(\text{Ba,Cs})_{1.33}(\text{Zn,Ti})_8\text{O}_{16}$ and $(\text{Ba,Cs})_{1.33}(\text{Ga,Ti})_8\text{O}_{16}$

R. Grote^a, T. Hong^a, L. Shuller-Nickles^{b,c}, J. Amoroso^d, M. Tang^e, K. Brinkman^{a,c,*}

^a Department of Materials Science and Engineering, Clemson, SC, USA.

^b Department of Environmental Engineering and Earth Sciences, Clemson, SC 29634, USA

^c Center for Nuclear Environmental Engineering Sciences and Radioactive Waste Management (NEESRWM), Clemson University, Clemson, SC, USA

^d Savannah River National Laboratory, Aiken, SC 29808, USA

^e Los Alamos National Laboratory, Los Alamos, New Mexico 87545, USA

*Corresponding author Tel: +1(864)656-1405; Email: ksbrink@clemson.edu

Abstract

The radiation damage tolerance of nuclear waste forms is dependent on the materials resistance to defect formation and its ability to accommodate the structural distortions that arise from defect formation. This study illustrates how the radiation tolerance of hollandite can be improved through compositional control of cesium stoichiometry. A hollandite series with the general form $\text{Ba}_x\text{Cs}_y\text{Zn}_{x+y/2}\text{Ti}_{8-x-y/2}\text{O}_{16}$ ($0 < x < 1.33$; $0 < y < 1.33$) was exposed to heavy ion (Kr^{2+}) irradiation at 27 °C, 100 °C, 200 °C and 300 °C followed by characterization with grazing incidence X-ray diffraction, transmission electron microscopy, and aqueous leaching tests. After exposure to 400 keV or 1 MeV Kr^{2+} irradiation, hollandite exhibited an onset of amorphization near 0.14 dpa and full amorphization ranging from 0.21 and 0.54 dpa depending on the cesium content. The radiation tolerance increased at elevated temperatures with a critical amorphization temperature between 200 °C and 300 °C. Elemental leaching decreased with increasing cesium content. Irradiated samples exhibited twice the fraction cesium release of pristine samples. Experimental results also showed that cesium release from irradiated samples was at a minimum for the $\text{Ba}_{0.33}\text{Cs}_{1.00}\text{Zn}_{0.83}\text{Ti}_{7.17}\text{O}_{16}$ sample.

Keywords

Hollandite; Radiation stability; Leaching; Cesium; Immobilization

1. Introduction

Hollandite is a promising material system for radioactive cesium (Cs) immobilization. The basic formula for hollandite is $\text{A}_2\text{B}_8\text{O}_{16}$, where A can be monovalent or divalent and B can be di-, tri-, tetra- or penta-valent depending on the chosen composition. The hollandite tunnel structure consists of four pairs of edge-sharing BO_6 octahedra. Neighboring pairs are connected at their corners forming a square. This

square framework repeats along the [001] direction forming a tunnel which accommodates the larger A-site cations. The majority of published work contains barium (Ba) in the A-site and titanium (Ti) in the B-site for nuclear waste immobilization. Cesium (Cs) is substituted into the A-site and di- or tri-valent cations are substituted into the B-sites to maintain charge neutrality in the system [1–4]. The hollandite crystal structure was first described in 1950 by Bystrom and proposed as a potential waste form for Cs immobilization by Ringwood et al. in 1979 [5,6]. Multiphase ceramic waste forms, such as SYNROC C, are one of the potential immobilization matrices under evaluation for commercial nuclear fuel reprocessing [6,7]. In these scenarios, Cs-containing hollandite will be one constituent phase in a multiphase system along with Sr-containing perovskite and actinide-containing pyrochlore and zirconolite phases [8]. All the constituent phases that make up this multiphase ceramic waste form have been shown to be thermodynamically stable [9-11]. Multiphase ceramic waste forms can be tailored to different waste streams to accommodate a wide range of waste elements. In many of the combined waste streams under consideration by domestic efforts by the Department of Energy's Nuclear Energy division for potential commercial fuel recycling, the hollandite phase represents a large fraction of the phase assemblage, typically in excess of 50% [7]. In these multiphase assemblages hollandite will be in contact with the other actinide-containing phases [12–14]. Therefore, the radiation stability of hollandite is an important factor to consider for material selection [15].

The radiation stability of hollandite has been previously studied by electron, neutron, and alpha irradiations, as well as accelerated heavy ions to simulate alpha-recoil damage [16–21]. For example, Kr^{2+} ions have been used to simulate alpha damage of constituent SYNROC phases, hollandite, zirconolite and perovskite [22,23]. Hollandite is susceptible to electronic defect formation in the form of oxygen interstitials and vacancies near Ti^{3+} ions when exposed to electron irradiation, used to simulate β and γ irradiation [17]. Similar electronic defects occur for both β^- and α , however structural damage more often occurs due to α -decay. Additionally, depending on the extent of exposure to heavy ion radiation, α particles, volume swelling, a tetragonal to monoclinic structural transition, and amorphization via crystalline disordering can occur [24]. Volume swelling of 2.1% with original crystallinity has been reported for hollandite irradiation by via alpha particles emitted from a PuO_2 source [25,26].

Crystalline disordering, or ion-induced amorphization, of hollandite occurs around 0.9 displacements per atom (dpa) with Kr^{2+} ions [3,26]. The amorphization process occurs by a damage cascade where the incident particle inelastically collides with lattice atoms transferring momentum and heat which lead to secondary defect formation [24,27]. All crystallinity in this cascade zone is disturbed then some fraction is recrystallized. If epitaxial recrystallization is incomplete then amorphous fraction forms and can accumulate upon subsequent irradiation. Further, electron irradiation stimulates the formation of oxygen

vacancies and tunnel displacement of Ba cations [17]. Most of these defects do not recombine upon annealing and some, such as Ti^{3+} and O^{2-} , migrate to form defect clusters [28]. In work by Kesson et. al, inclusion of Ar^+ ions in tunnels along with Ba^{2+} depletion was suggested to cause tunnel distortion and octahedral framework collapse [29]. Studies of the amorphization behavior at elevated temperatures have been performed on pyrochlore based waste form materials but not hollandite systems [26,27,30]. For waste form materials there exists a critical temperature at which full recrystallization occurs within the cascade making the material highly resistant to radiation damage. The critical amorphization temperature varies between materials and has not been determined for hollandite.

While the composition of the B-site cation has been shown to effect the radiation tolerance, the impact of the A-site cation composition has not been reported in literature. The emergence of an amorphous phase has been shown in crystalline/amorphous cross-sections of irradiated for Cr- and Cr,Al,Fe-hollandites [3]. Grazing incidence X-ray diffraction (GIXRD) measurements of the amorphous region reveal a broad peak from 22° to 37° in the diffraction spectra [3]. The thickness of the amorphous layer is dependent on the ionizing energy and material composition and is often a few hundred nanometers thick. GIXRD is especially useful in examining the amorphous layer as it can probe 50nm thick layers of the surface depending on the incidence angle [3,31]. Amorphization is caused by the cumulative buildup of point defects in ionic structures such as hollandite. Preventing the buildup of these point defects or recovering via frenkel pair recombination is key to a materials resistance to amorphization [32].

In hollandite, there exists a superlattice ordering phenomena has been observed and is associated with tunnel cation ordering [1,2,29,34,35]. The four primary factors when considering the superlattice ordering phenomena are intra-tunnel interactions, inter-tunnel interactions, octahedral shielding capacity, and kinetic effects. Intra-tunnel interactions arise via electrostatic repulsion between adjacent tunnel cations limiting full A-site (or tunnel) occupancy for compositions containing divalent tunnel cations [29,34]. According to Bayer and Hoffman, full tunnel occupancy can be achieved only for titanate hollandites containing Rb^+ or K^+ , as their atomic radii and charge density are sufficiently small to avoid steric and electronic hindrances [35]. Though Cs is monovalent, its atomic size does not allow for full occupancy due to steric interference. A related intra-tunnel interaction is cation displacement ordering that can occur where tunnel cations are regularly displaced off the lattice site leading to superlattice ordering [29]. Intertunnel interactions between cations from adjacent tunnels that can lead to three dimensional superlattice ordering [36]. In particular, Ba-hollandite often adopts a three dimensional tunnel ordering due to higher A-site charge density that must overcome the electrostatic shielding of the octahedral framework. The tunnel ordering pattern for a three-dimensionally ordered structure is typically offset

relative to the neighboring tunnel to reduce inter-tunnel repulsion. The shielding capacity of the octahedral framework imperfectly limits the long-range effect of inter-tunnel interactions and can be determined by the polarizability of the given octahedral framework. In general, smaller high valence ions (*e.g.*, Ti^{4+}) have greater polarizability than larger low valence ions (*e.g.*, Zn^{2+}). Finally, kinetic effects suggest that crystallization from a melt adopts longer range ordering than crystallization from a sub-solidus temperature (*i.e.*, solid state synthesis) [29]. For the current study all samples were crystallized sub-solidus so the kinetic effect should be minimized. Nonstoichiometric oxygen content has been shown to affect the temperature of the monoclinic/tetragonal symmetry transition and superstructure reflections in Ba,Ti-hollandite with maximum superstructure reflection intensity for ideal oxygen stoichiometry and no superstructure reflections for samples with significant oxygen excess [37].

Ultimately, changes in the crystalline structure induced by alpha irradiation can impact the chemical durability of ceramic waste forms over long periods of time. Leaching studies using ASTM C 1285 product consistency test (PCT), which measures elemental release from crushed powder at an elevated temperature, and ASTM C 1220 leach test, which measures elemental release from a monolith at an elevated temperature have been performed separately on hollandite and other constituent phases in SYNROC [11, 38, 39]. For example, leach rates below 10^{-2} g/m²/day were measured for Ca, Nd, Tc, U, and Pu from multiphase SYNROC phases [40,41] and are below the reported leaching rates for hollandite, which have been measured to between 10^{-2} and 10^{-1} g/m²/day [42,43]. This indicates that improvement of hollandite leaching durability would lead to a noticeable improvement in waste form performance [44].

To our knowledge, the only published study on the leaching behavior of irradiated hollandite was performed in the presence of gamma irradiation, which had no significant effect on hollandite leaching behavior [45]. In this work, the effect of alpha decay damage on hollandite was simulated by heavy ion irradiation and the subsequent impact on elemental leaching of have been studied together. The purpose of this study is to investigate the effect of Cs incorporation on the radiation tolerance of hollandite with the goal of developing more resilient and efficient nuclear waste forms.

2. Experimental

2.1. Processing and sample preparation

The Zn-hollandite samples of the general form $\text{Ba}_x\text{Cs}_y\text{Zn}_{x+y/2}\text{Ti}_{8-x-y/2}\text{O}_{16}$ ($0 < x < 1.33$; $0 < y < 1.33$) were synthesized from BaCO_3 , Cs_2CO_3 , ZnO , and TiO_2 and ball milled in ethanol before undergoing a solid state reaction in air. Two sets of Zn-hollandite samples with identical target compositions were tested. The first set followed the processing conditions outlined in Grote et. al [11]. However, the second set

contained 15 at% excess Cs to compensate for Cs loss during processing and was calcined at 1225°C for 10 hours twice then sintered at 1300°C for 1 hour. The altered processing routine for the second experiment was found to eliminate the secondary rutile phase and reduce Cs loss as has previously been reported in [11]. All samples were characterized by XRD and EDX to confirm structure and composition. The Ga-hollandite samples were prepared in the same manner as Xu et al. [46]. *Ex situ* monolith specimens were prepared from sintered samples. The samples surfaces were polished using 3 μm lapping film. *In situ* specimens were prepared by ball milling the sintered powder with yttria-stabilized zirconia for 24 hours. Then powder was suspended in an ethanol solution and a drop of the solution was allowed to rest on perforated carbon film for two minutes before being dried off. The edges of thin particles were selected for observation so that full penetration by the ion beam was achieved. A range of Cs doping was chosen for this work to investigate how the thermal and structural stabilizing effects induced by Cs incorporation have an impact on radiation tolerance [11,47]. Ga-hollandite was also tested to see how radiation tolerance changes with a smaller radius higher valence B-site dopant.

Eleven compositions were prepared to study the effect of Cs content on the critical radiation dose required for amorphization. In Table 1, the sample list is given with associated target and energy dispersive X-ray spectroscopy (EDX) measured stoichiometry. All samples had densities ranging from 85-90% of the theoretical density and formed with tetragonal, $I4/m$, symmetry except for Ba133Zn-2, which was monoclinic, $I2/m$. In this study, the oxygen stoichiometry was assumed to be ideal as it was processed in air, and the Ti stoichiometry was assumed to remain unchanged from the targeted value. The real stoichiometry was charge balanced by multiplying the Ba, Cs and Zn EDX stoichiometries by a normalization factor, determined using Equation 1. The normalization factor was calculated from the EDX stoichiometry of each element, N_i , and the elements charge, Q_i .

$$(Q_o * N_o - Q_{Ti} * N_{Ti}) / (N_{Ba} * Q_{Ba} + N_{Cs} * Q_{Cs} + N_{Zn} * Q_{Zn}) = \text{normalization factor} \quad \text{Equation 1}$$

The first set of Zn samples were tested *in situ* at Argonne National Laboratory (ANL) using a 1 MeV Kr²⁺ source and *ex situ* at Los Alamos National Laboratory (LANL) using a 400 keV Kr²⁺ source. The Ga samples were tested *in situ* at ANL with a 1 MeV Kr²⁺ source. The second set of Zn samples were only tested with the *in situ* transmission electron microscopy (TEM) at ANL (1 MeV Kr²⁺) to reproduce the results of the previous tests and to confirm the Cs067Zn-1 results.

Table 1. Sample compositions used for these experiments. The compositions from the second set contained 15% excess Cs to compensate for Cs losses during processing. Compositons with * were used for leaching

Short Name	Target Composition	EDX Composition
Cs000Zn-2	Ba _{1.33} Zn _{1.33} Ti _{6.67} O ₁₆	Ba _{1.26} Cs _{0.00} Zn _{1.41} Ti _{6.67} O ₁₆

Cs024Zn-1*	Ba _{1.04} Cs _{0.24} Zn _{1.16} Ti _{6.84} O ₁₆	Ba _{1.15} Cs _{0.15} Zn _{1.09} Ti _{6.84} O ₁₆
Cs029Zn-2*	Ba _{1.04} Cs _{0.29} Zn _{1.19} Ti _{6.81} O ₁₆	Ba _{0.91} Cs _{0.30} Zn _{1.31} Ti _{6.81} O ₁₆
Cs067Zn-1*	Ba _{0.67} Cs _{0.67} Zn _{1.00} Ti _{7.00} O ₁₆	Ba _{0.65} Cs _{0.51} Zn _{0.84} Ti _{7.00} O ₁₆
Cs067Zn-2*	Ba _{0.67} Cs _{0.67} Zn _{1.00} Ti _{7.00} O ₁₆	Ba _{0.49} Cs _{0.71} Zn _{1.15} Ti _{7.00} O ₁₆
Cs100Zn-1	Ba _{0.33} Cs _{1.00} Zn _{0.83} Ti _{7.17} O ₁₆	Ba _{0.53} Cs _{0.50} Zn _{0.89} Ti _{7.17} O ₁₆
Cs100Zn-2*	Ba _{0.33} Cs _{1.00} Zn _{0.83} Ti _{7.17} O ₁₆	Ba _{0.32} Cs _{1.01} Zn _{0.84} Ti _{7.17} O ₁₆
Cs133Zn-1*	Cs _{1.33} Zn _{0.67} Ti _{7.33} O ₁₆	Ba _{0.00} Cs _{1.32} Zn _{0.68} Ti _{7.33} O ₁₆
Cs133Zn-2*	Cs _{1.33} Zn _{0.67} Ti _{7.33} O ₁₆	Ba _{0.00} Cs _{1.42} Zn _{0.63} Ti _{7.33} O ₁₆
Cs067Ga	Ba _{0.67} Cs _{0.67} Ga _{2.00} Ti _{6.00} O ₁₆	Ba _{0.77} Cs _{0.53} Ga _{2.06} Ti _{6.00} O ₁₆ [48]
Cs133Ga	Cs _{1.33} Ga _{1.33} Ti _{6.67} O ₁₆	Cs _{1.22} Ga _{1.44} Ti _{6.67} O ₁₆ [48]

2.2. SRIM modeling

The SRIM program was used to model the radiation dose and convert ion fluences into dpa [49]. The SRIM model is shown below in Figure 4.1. An assumed displacement energy threshold of 40 eV was used for all elements. Kr²⁺ ions with an energy of 1 MeV were calculated to have a range of 700 nm, fully penetrating the 100-200 nm thin samples. The average dpa between 100-200 nm was 0.14 dpa for 1x10¹⁴ fluence and 0.69 dpa for 5x10¹⁴ fluence. The 400 keV Kr²⁺ ions had a range of about 300 nm with a max dpa of 0.21 dpa for 1x10¹⁴ fluence and 1.06 dpa for 5x10¹⁴ fluence.

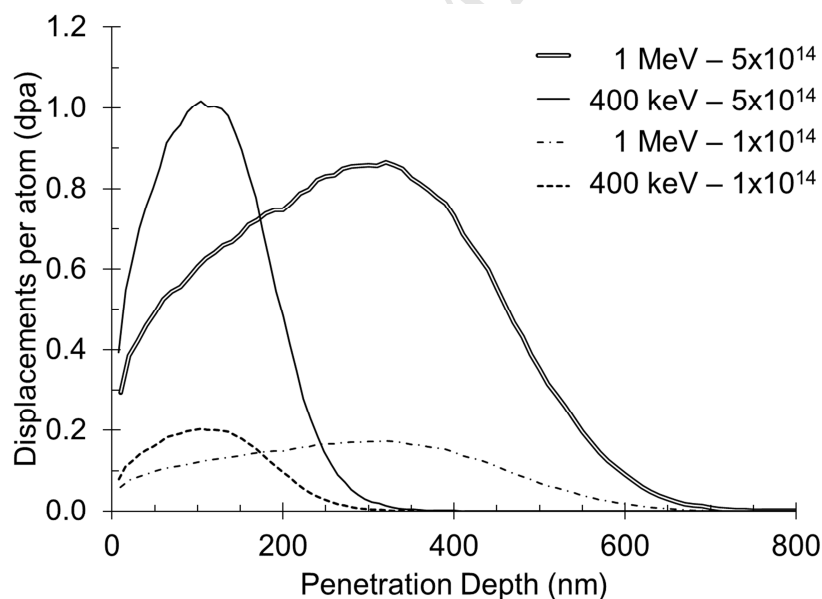


Figure 1. SRIM dpa calculation for Cs067Zn that was exposed to 1x10¹⁴ or 5x10¹⁴ Kr/cm² fluence using either 400 keV ions with an incidence angle of 0° or 1 MeV ions with a incidence angle of 15°

2.3. *In situ* irradiation and characterization

In situ ion irradiation experiments were performed at ANL in the intermediate voltage electron microscope (IVEM) at room temperature (~27 °C), 100 °C, 200 °C and 300 °C using Kr²⁺ ions accelerated

at 500 keV resulting in an effective voltage of 1 MeV. The IVEM lab at the ANL has a Tandem ion accelerator attached to a Hitachi H-9000NAR microscope with a double-tilt stage ($\pm 30^\circ$) operating at 300 kV. Selected-area electron diffraction (SAED) patterns were recorded before irradiation and periodically during irradiation until full amorphization was reached. The electron beam was turned off during ion irradiation to avoid concurrent electron irradiation damage. Due to the equipment setup the ion beam was angled at 15° to the sample's normal vector. After each irradiation step of 5×10^{13} Kr/cm² the SAED patterns were realigned along the zone axis and imaged.

2.4. *Ex situ* irradiation and characterization

Ex situ ion irradiation experiments were performed at room temperature at the Ion Beam Materials Laboratory (IBML) at Los Alamos National Laboratory (LANL) using 200 kV Danfysik high current research ion implanter. Kr²⁺ ions were accelerated to an effective ion voltage of 400 keV. Four compositions, Cs024, Cs067, Cs100, and Cs133 were compared at fluences of 1×10^{14} or 5×10^{14} Kr/cm² to study the heavy ion irradiation effects. The samples were characterized by grazing incidence X-ray diffraction (GIXRD) and TEM. GIXRD measurements were made by Bruker AXS D8 Advanced X-ray diffractometer with Cu K α radiation. The 2θ angle was variable while a 0.5° angle of incidence (aoi) to the sample was fixed. The scan range was from 10 - 80° with a step size of 0.02° and a step rate of 0.5° per second. The x-ray penetration depth¹ for a 45 keV Cu anode at 0.5° aoi was less than 50 nm which is significantly less than Kr range of ~ 250 nm [3]. A comparison XRD measurement with an aoi of 0.25° was also performed. The results were not significantly different therefore and aoi of 0.5° was used. The *ex situ* irradiated samples were also prepared for cross-sectional TEM analysis using the focused-ion beam (FIB) *in situ* lift out method. The radiation induced microstructure was examined by Hitachi H-9000 TEM operating at 300 kV. The percent of amorphization was determined by the dividing the integral of the amorphous peak, which is the area under the curve from 24 - 32° , by the total area (crystalline + amorphous peaks) of the spectra [50-52].

2.5. Leaching procedure

The ASTM C 1220 leach test method was used to quantify elemental release from monolithic specimens [53]. Each composition was measured in duplicate using samples with dimensions approximately 8mm x 8mm x 2mm. The samples were combined with de-ionized water (~ 15 ml) to maintain a constant surface area to volume (S/V) ratio (13 mm²/ml) for all samples. Crushed powder standards were also prepared and tested alongside the monoliths. All samples and standards were washed

¹ The penetration depth was calculated from the linear absorption coefficient, μ , that was calculated by using the mass attenuation coefficients, μ/ρ , from each element in the compound

and dried according to the procedure, loaded into sealed stainless steel pressure vessels, sealed with threaded enclosures, and heated at $\sim 90^{\circ}\text{C}$ for ~ 7 days. Subsequently, the vessels were cooled and the leachates were filtered, acidified, and measured for elemental composition using inductively coupled plasma mass spectrometry (ICP-MS). The concentration of elements in the leachates were compared to the elemental concentrations in the un-leached samples that were measured using EDX to obtain a fraction loss for each element. ICP-MS was performed to confirm EDX compositional analysis and the compositions stoichiometries were charge balanced via Equation 7. Both the geometric surface area and BET were used to measure surface area and correct for surface porosity to obtain a normalized release rate for each composition.

3. Results

All eleven Zn-hollandite and Ga-hollandite samples were examined by the *in situ* irradiation method described in the experimental section. The SAED patterns were then analyzed by comparing the presence of an amorphous halo and determining the fluence at which the sample became fully amorphous. Four Cs-Zn-hollandite compositions were examined *ex situ* in duplicate by GIXRD after Kr^{2+} irradiation – Cs_{0.24}Zn-1, Cs_{0.67}Zn-1, Cs_{1.00}Zn-1, and Cs_{1.33}Zn-1. GIXRD of each sample was collected before irradiation, after 1×10^{14} Kr/cm² or 5×10^{14} Kr/cm² irradiation.

3.1 *In situ* Kr irradiation on Zn-hollandites at room temperature

TEM SAED patterns of pristine samples of Zn-hollandite prior to irradiation exhibited a highly crystalline phase, corresponding to tetragonal or monoclinic, with secondary reflections attributed to A-site tunnel ordering (top row of Figure 2). The Ba end member exhibited tunnel ordering in its XRD pattern, which has been reported in other hollandite systems [2]. Irradiation with 1 MeV Kr^{2+} ions to a fluence of 1×10^{14} Kr/cm² fluence (0.14 dpa) resulted in the formation of an amorphous ring for all compositions investigated. Additionally, there was a decrease in spot intensity due to a reduction of long range ordering. The Ba_{1.33}Zn composition exhibited faster than average onset of amorphization by 5×10^{13} fluence (0.09 dpa), however this was a minor qualitative observation. The Cs-rich compositions, $Cs \geq 1.00$, maintained higher crystallinity after exposure to a fluence of 1.5×10^{14} Kr/cm² than the Cs poor compositions, $Cs \leq 0.29$, as seen in SAED patterns in the second row of Figure 2. The fluence required for full amorphization also increased with Cs content showing that high Cs content hollandite compositions can improve the radiation tolerance by about 100% compared to the Ba-hollandite end member. The increased radiation tolerance may be attributed to structural factors including reduction in atomic displacements due to the larger unit cell of the Cs end member, a more rigid tunnel structure requiring a larger activation energy for displacement and shorter displacement distance for Cs vs Ba.

Table 2. Amorphization doses for Zn-doped samples irradiated *in situ* at ANL with a 1 MeV Kr²⁺ ion beam. The average onset of amorphization and full amorphization fluence and calculated dpa are given for each composition

Short Name	Composition	Amorphization onset (Kr/cm ²)/(dpa)	Amorphization full (Kr/cm ²)/(dpa)
Ba133Zn	Ba _{1.33} Zn _{1.33} Ti _{6.67} O ₁₆	0.83 x 10 ¹⁴ /(0.114)	1.50 x 10 ¹⁴ /(0.206)
Cs029Zn	Ba _{1.04} Cs _{0.29} Zn _{1.19} Ti _{6.81} O ₁₆	1.00 x 10 ¹⁴ /(0.137)	1.83 x 10 ¹⁴ /(0.251)
Cs067Zn	Ba _{0.67} Cs _{0.67} Zn _{1.00} Ti _{7.00} O ₁₆	1.00 x 10 ¹⁴ /(0.137)	2.00 x 10 ¹⁴ /(0.274)
Cs100Zn	Ba _{0.33} Cs _{1.00} Zn _{0.83} Ti _{7.17} O ₁₆	1.13 x 10 ¹⁴ /(0.155)	2.50 x 10 ¹⁴ /(0.343)
Cs133Zn	Cs _{1.33} Zn _{0.67} Ti _{7.33} O ₁₆	1.17 x 10 ¹⁴ /(0.161)	3.92 x 10 ¹⁴ /(0.538)

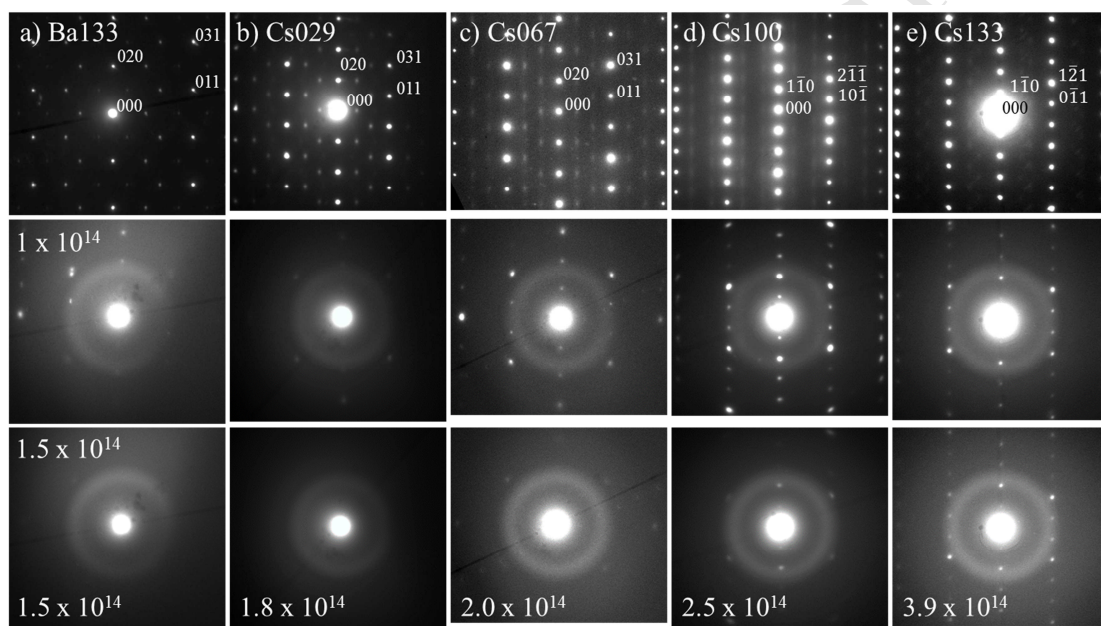
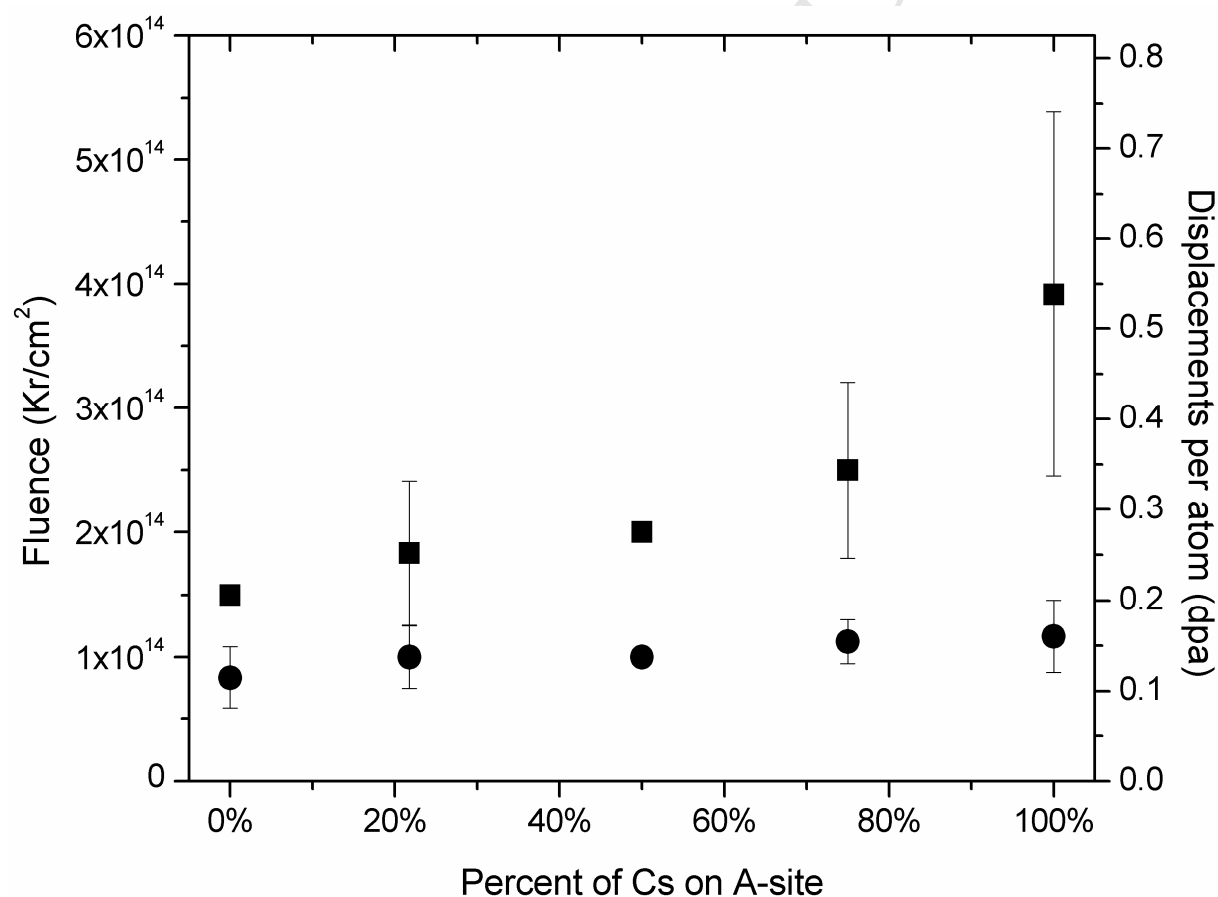


Figure 2. SAED of each composition during the *in situ* irradiation tests along their respective zone axis; a) Ba133 along [100], b) Cs029 along [100] c) Cs067 along [100] d) Cs100 along [111] and e) Cs133 along [111]. For comparison the amorphization at 1×10^{14} Kr/cm² (middle row) and 1.5×10^{14} has been shown as well as the fluence required for full amorphization is noted in the bottom right corner

The dose (in fluence and dpa) required for onset and full amorphization is further compared in Fig. 3. The onset amorphization was nearly constant at 1×10^{14} Kr/cm² (0.17 dpa) across the compositional range with the Cs rich compositions onset slightly higher by 2.5×10^{13} Kr/cm² (0.04 dpa). This increase in amorphization onset for Cs100 and Cs133 was negligible when compared to the irradiation required for full amorphization. Full amorphization increased from 1.5×10^{14} Kr/cm² (0.21) to 4×10^{14} Kr/cm² (0.54 dpa) as Cs content increased.

The *in situ* TEM SAEDs verified that the amorphous halo onset varied slightly between compositions however the critical fluence required for full amorphization increased by 160% across the compositional range. This increase in critical amorphization dose show that high Cs content hollandite compositions were more stable. There are multiple contributing factors for the rise in critical dose the most important are summarized in the following. First, as Cs content increases the unit cell increases. A larger unit cell will limit the number of atoms being displaced far enough to form defects and a more stable tetragonal structure requires greater activation energy for displacement. Secondly, the Cs ion is significantly larger than the Ba ion so a displaced Cs will both require more energy for displacement and interact with more atoms which limit the displacement distance. Finally, doping with Cs has been shown to stabilize the tetragonal symmetry [11,45]. Therefore, a high Cs content tetragonal structure will require more defects



to be distorted than a monoclinic structure.

Figure 3. Onset and full amorphization across the compositional range. Circle: Average of onset of amorphization fluence with 95% standard deviation error bars, Square: Average of full amorphization fluence with 95% standard deviation error bars

3.2 *In situ* Kr irradiation on Zn-hollandites at elevated temperature

Three temperatures were selected to determine the effect of temperature on amorphization. As commonly seen in other waste forms, Zn-hollandite exhibited a critical temperature at which the dose for amorphization increased drastically. In Figure 4.4, the compositional dependence of the critical amorphization dose as a function of temperature is compared for Cs029, Cs067, and Cs133. For all three compositions the critical amorphization dose significantly increased between 200 °C and 300 °C. This is believed to be due to increased defect mobility at 300 °C resulting in a higher rate of defect recombination (annealing). At 100 °C each composition exhibited an increase in critical amorphization dose over the room temperature measurements. At 200 °C the critical amorphization dose for the Cs133 sample had tripled while the Cs029 and Cs067 samples exhibited negligible changes. At 300 °C, all samples exhibited a significant increase in their critical amorphization dose with Cs029 at about 1.7 dpa while Cs067 and Cs133 remained crystalline until about 4 dpa. From these results it is clear that defect recovery plays a significant role in the prevention of amorphous phase formation especially at temperatures above 200 °C. The difference in the critical amorphization dose for Cs133 at 200 °C was due to its more homogenous structure. Defect recovery and recrystallization would be easier without a mixed A-site and less Zn on the B-site. Our new experimental results show that radiation-induced phase transformations in hollandite progress from a tetragonal structure to a monoclinic structure at a low radiation dose and finally to an amorphous phase at a high dose [Ming Tang et al., unpublished results].

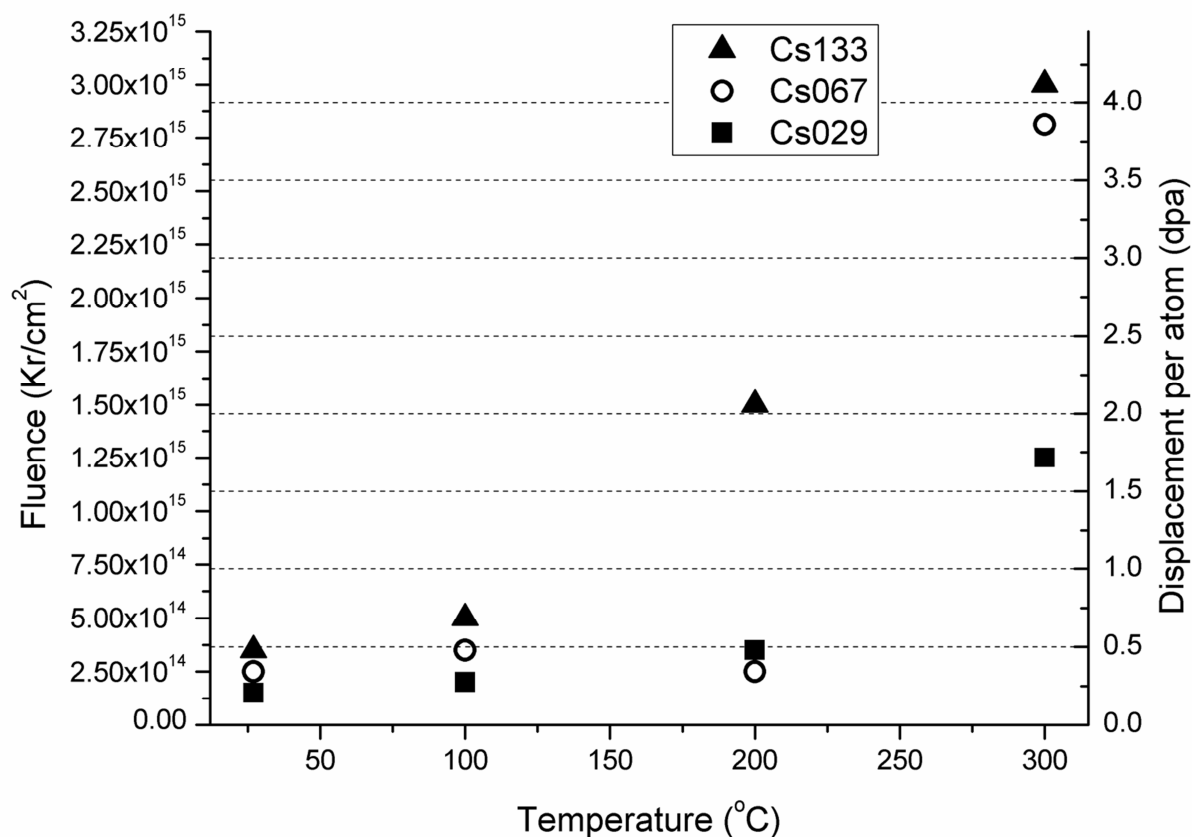


Figure 4. Critical amorphization dose for each composition at each temperature. Square: Cs029, Circle: Cs067, and Triangle: Cs133

The process by which the structural amorphization occurs from α -decay events is by the accumulation of simple Frenkel defects and amorphous, or aperiodic, regions that result in the loss of long range order [3,54]. The likely defect growth process which results in degradation of crystal structure periodicity is describe in Fig. 5. The mechanism for defect growth was likely tunnel collapse caused by Frenkel pair formation from cation displacement. This assumes there was limited solid state diffusion at room temperature and the compositions are close to the minimum limit for tunnel occupancy. This minimum occupancy is based on bulk hollandite properties [55].

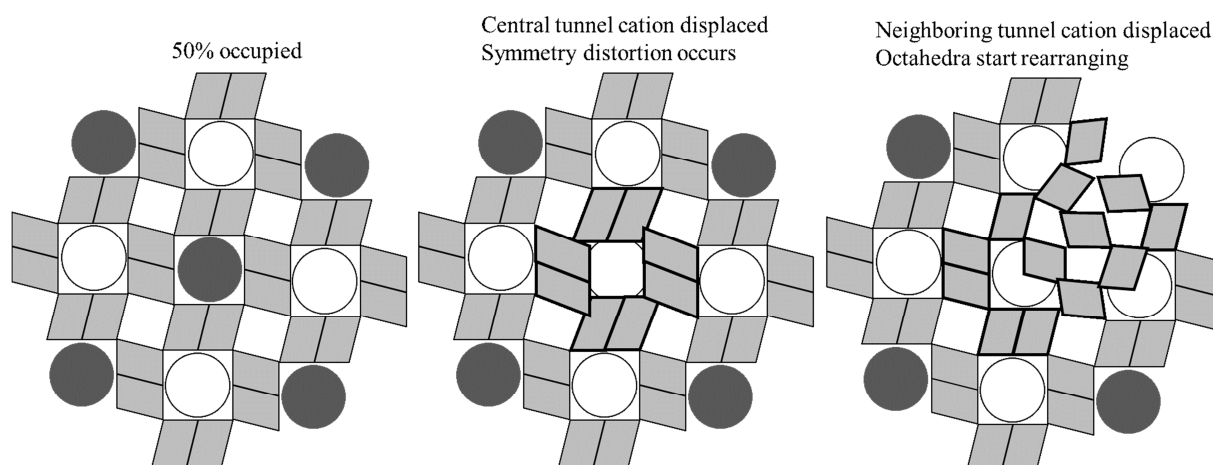


Figure 5. Schematic depicting proposed mechanism for tunnel collapse in response to irradiation induced frenkel defect formation in hollandite

A lesson from the tetragonal or monoclinic symmetry discussion in the literature can be applied here. When the tunnel cation becomes smaller than its cavity the cation can be displaced off its $4/m$ special position [36]. This displacement enables the octahedra to undergo a twisting distortion in order to accommodate the minimum energy of the displaced cation. Distortion of the octahedral wall lowers the symmetry to monoclinic. In Fig. 5, with 50% A-site occupancy each tunnel cation is responsible for stabilizing the neighboring six unoccupied tunnel sites. In order to form an amorphous or disordered zone the required local defect concentration is dependent on whether or not the free energy of an irradiation damaged region exceeds the free energy of the amorphous metastable state. If the lower limit for occupancy in a local area is passed then it is reasonable to assume that the octahedra will distort to compensate for the lack of the repulsive tunnel force. If the surrounding tunnels cannot accommodate a monoclinic distortion then the tunnel will collapse resulting in amorphous or disordered zone. The point where these local amorphous zones overlap can be considered an amorphous phase. The growth of the amorphous phase depends on the presence of unstable neighboring tunnels collapsing and being incorporated into the amorphous phase.

The defect concentration required to trigger an amorphization is directly linked to the displacement cascade caused by irradiation. Irradiation induced displacement cascades in ceramic structures similar to hollandite are typically heterogeneous and follow direct impact or cascade overlap models [30,56]. The direct impact model is where amorphization occurs in an affected region along the path of a heavy ion, such as an α -decay recoil nucleus. While for the cascade overlap model an amorphous phase forms where affected regions, from two particles, overlap. In this study, the persistent crystalline structure and delay in amorphization onset, seen in Fig. 2, as well as the behavior of amorphous phase formation in relation to dose, shown in Fig., suggest a combination of the direct impact and cascade overlap models.

The results from the temperature dependence irradiation experiment suggest a combined direct impact/cascade overlap amorphization model. This model seems reasonable as the onset of amorphization was $\sim 1 \times 10^{14}$ Kr/cm² for all samples at all temperatures. However, at higher temperatures, near 300°C, the critical dose for full amorphization increased dramatically. This can be explained by the incident particle causing amorphization near its path but higher defect mobility is sufficiently great to limit amorphization from secondary recoil collisions. As the temperature decreased the defect mobility, and therefore recombination rate, decreased; such that, the damage from secondary collisions was metastable. When these metastable damaged regions overlap a stable amorphous phase would form.

3.3 *In situ* Kr irradiation on Ga-hollandite

Two Ga samples were irradiated in conjunction with the Zn-doped system to compare how different B-site dopants affect the radiation tolerance. Both Ba_{0.67}Cs_{0.67}Ga_{2.00}Ti_{6.00}O₁₆ and Cs_{1.33}Ga_{1.33}Ti_{6.67}O₁₆ were tested. The Ga-hollandite results shown in Table 3 support the hypothesis that additional Cs increases the radiation tolerance of hollandite. Additionally, the Ga-doped samples appear to have a higher radiation tolerance than the Zn-doped samples. The higher tolerance can be explained by easier defect recombination due to a more similar B-site dopant. Compared to Zn²⁺, Ga³⁺ is more similar to Ti⁴⁺ in both its atomic radius and charge density which would reduce the octahedral strain. The impact of B-site dopant effects are preliminary and additional work is required to confirm the observed trends.

Table 3. Ga doped samples irradiated *in situ* at room temperature at ANL. The onset of amorphization and full amorphization fluence and calculated dpa

Short Name	Composition	Amorphization onset (Kr/cm ²)/(dpa)	Amorphization full (Kr/cm ²)/dpa
Cs067Ga	Ba _{0.67} Cs _{0.67} Ga _{2.00} Ti _{6.00} O ₁₆	$1.00 \times 10^{14}/(0.18)$	$1.50 \times 10^{14}/(0.26)$
Cs133Ga	Cs _{1.33} Ga _{1.33} Ti _{6.67} O ₁₆	$2.00 \times 10^{14}/(0.35)$	$1.00 \times 10^{15}/(1.76)$

3.4 *Ex situ* Kr irradiation on hollandite

Figure 6 shows the GIXRD patterns for the Cs100-Zn hollandite composition before and after 400 keV Kr irradiation. The pristine spectra indicates a single phase hollandite structure. After 5×10^{14} Kr/cm² a definite amorphous peak had formed. Additionally, residual hollandite peaks remained with diminished intensity after irradiation. In some cases the abnormal changes in peak intensity are caused by texturing, where residual crystals are oriented in similar directions. However, hollandite recrystallization during irradiation could also cause the residual peaks. The remaining hollandite peaks for the 1×10^{14} Kr/cm² samples are likely due to residual hollandite crystalline regions as the *in situ* experiment showed a crystalline SAED pattern at a similar dpa. The remaining hollandite peaks after 5×10^{14} Kr/cm² are likely

due to either recrystallization or texturing as *in situ* SAED patterns were fully amorphous at a similar dpa. It is unlikely these peaks are due to residual crystallites with different compositions than the hollandite phase as the peak locations are identical to hollandite and though these compositions are complex the only secondary phase present prior to irradiation was TiO₂.

In Figure 7, the amorphous fraction vs. Cs content of all four compositions for both 1×10^{14} and 5×10^{14} Kr/cm² have been calculated. Based off the *in situ* results the amorphous fraction was expected to be the same for all compositions after 1×10^{14} Kr/cm² as all compositions experience amorphous onset near 1×10^{14} Kr/cm². The amorphous content was also expected to increase after 5×10^{14} Kr/cm² with the low Cs content samples having a higher amorphous fraction. Overall the growth of the amorphous fraction followed expectations. However, the amorphous fraction analysis indicated that the intermediate compositions, not the higher Cs content samples, had a lowest amount of amorphous phase formation with the Cs133 end member having the highest amorphous fraction.

These results appear to contradict the *in situ* TEM results as the amorphous fraction did not directly relate to the Cs content. However, this excludes the differences between surface and whole particle measurements as well as the absence of a control spectra to standardize the amorphous fraction calculation. TEM focuses on a single grain, where the density is very close to its theoretical limit and there are no surface roughness or orientation effects. In contrast, for a surface sensitive measurement, such as GIXRD, the surface roughness is an important factor to consider as the samples were 85-90% dense. Therefore depending on the surface orientation the X-rays could penetrate much further than calculated. The independent amorphous content results and variation seen between spectra of the same sample could be due to surface roughness and lower density skewing the amorphous content results.

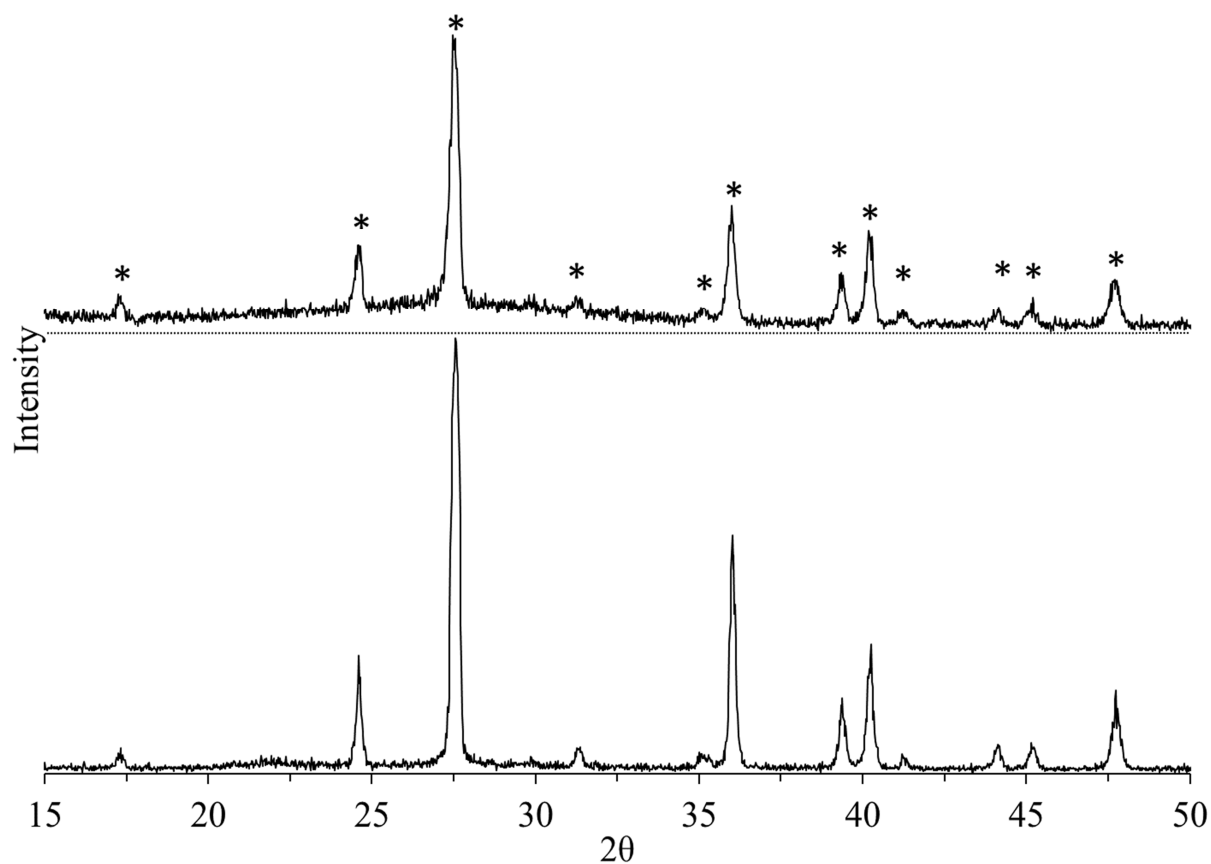


Figure 6. GIXRD of Cs₁₀₀Zn-1 which shows the broad amorphous peak from 24° to 32° and the residual crystalline structure. The bottom spectra was collected before irradiation while the top spectra was collected after 5 × 10¹⁴ Kr/cm² with a black dotted line indicating the baseline. The * identify hollandite structure peaks

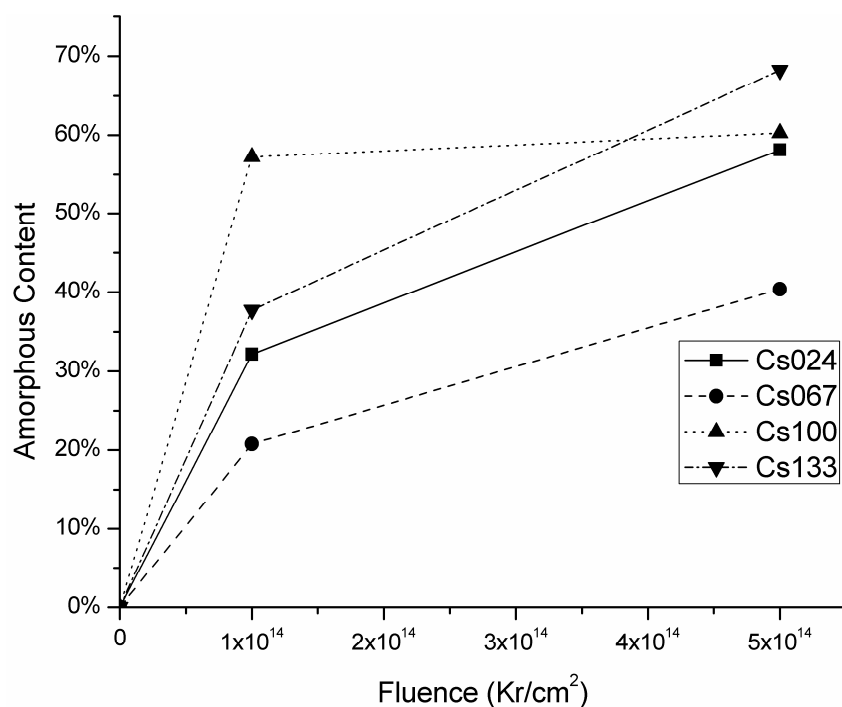


Figure 7. Percent amorphous versus fluence showing how the amorphous content increased with dose

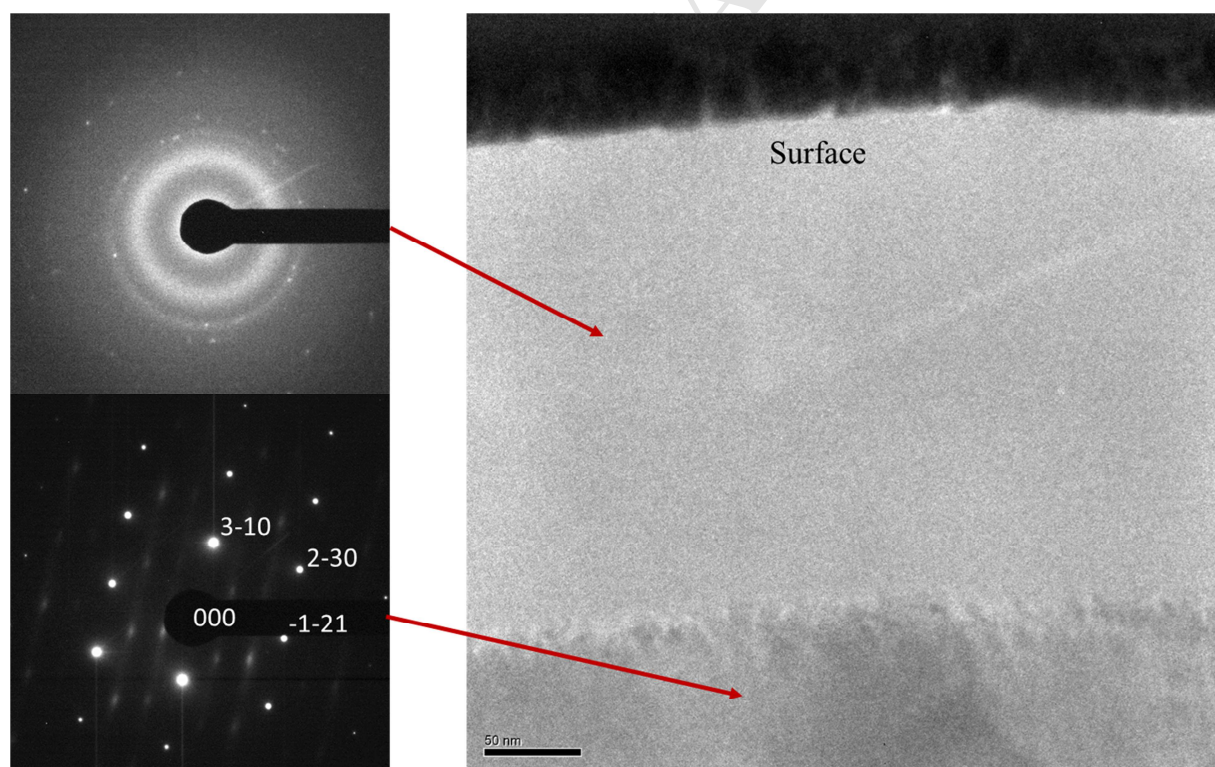


Figure 8. Selected area electron diffraction (left) and TEM bright field image (right) of Cs100 sample, along [137], irradiated to 5×10^{14} Kr/cm². The dark layer at the top is a carbon coating from the FIB process

The Cs100Zn-1 cross-section of the radiation affected regions shown in Fig. 8 revealed an amorphous layer thickness of approximately 250 nm with no residual crystalline pattern. At a depth of 250 nm the structural damage is equivalent to ~ 0.14 dpa, which is the same dpa required for the amorphous onset seen in the *in situ* experiment. Therefore, the SRIM damage model agreed well with the thickness of the amorphous layer measured in the cross-section. Fig. 8 confirms the amorphous phase and shows that the amorphous layer thickness can be predicted from the amorphization onset dpa using SRIM dpa depth.

3.5 Superlattice order to disorder transformation prior to amorphization

Superlattice ordering has been reported in hollandite literature from XRD and TEM studies [1,2,29,33,34]. In Fig. 9, an order to disorder transformation of the superlattice pattern occurs around 5×10^{13} Kr/cm² slightly before the onset of amorphization. Amorphization of the superlattice pattern is caused by a disruption of the tunnel cation offset and vacancy ordering which are necessary to create the superlattice. The tunnel takes up about half the cross-sectional area and due to the regular vacancies allowing for unimpeded displacement is one of the lower energy pathways for displacement propagation. It is reasonable to expect the superlattice pattern to be interrupted before the structure initially starts amorphization. The probable mechanism for the order-disorder transformation was tunnel cation displacement along the tunnel. While tunnel displacement would not cause an amorphous halo in the SAED pattern, the tunnel displacement would have a significant impact on the superlattice reflections (noted as $(00\frac{1}{3})$ and $(01\frac{2}{3})$) explaining why the superlattice spot intensity decreases rather quickly.

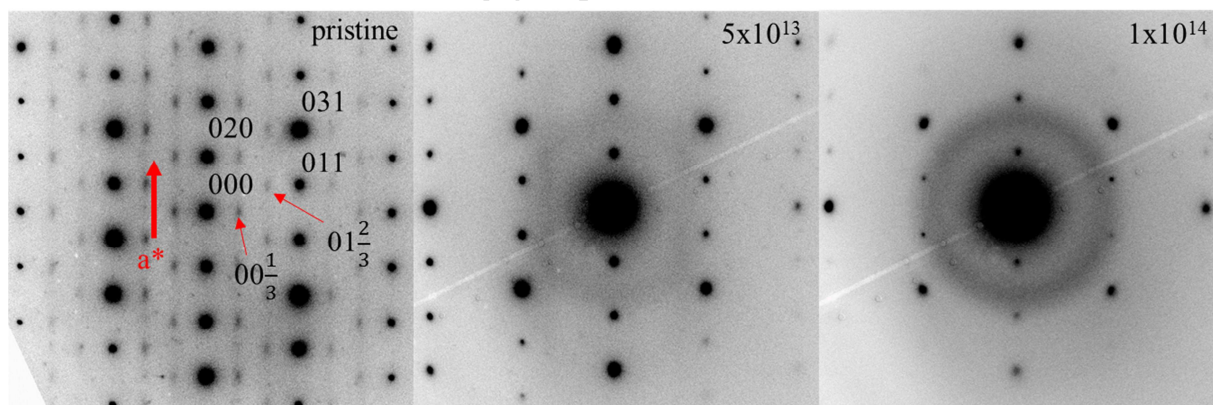


Figure 9. These SAED patterns are of Cs067Zn-2 along the [100] zone axis. From left to right, pristine, 5×10^{13} and 1×10^{14} . The superlattice reflections, identified by the red arrow, in-between each primary line disappeared after 5×10^{13} irradiation

3.6 Irradiated Sample Leaching Measurements

The fractional and normalized release of Cs for individual replicates from the particle and monolith leach testing is summarized in Figure 10. As noted in Grote et al. hollandite elemental release is affected

by its Cs content, where higher Cs content compositions exhibit lower elemental release [11]. A similar behavior also occurs for the irradiated samples and indicates that the Cs stoichiometry in hollandite limits elemental release. Irradiation resulted in a 100 to 200% increase in fractional Cs release as seen in Figure 10 a). A notable exception was irradiated Cs133, which had the highest Cs release. Leaching of the irradiated Cs133 end member was an anomaly by releasing ~8x the fractional Cs leaching as the irradiated Cs100 and unirradiated Cs133 samples. While all samples exhibited higher surface area after irradiation, Cs133 also had a bimodal grain structure and particularly rough surface. Conversely, Zn leaching from the Cs133 sample was less than all other irradiated samples even though Cs leaching was much higher. This may be indicative of tunnel collapse without breakdown of the octahedra and the slower water solubility of Ba slowing Cs diffusion.

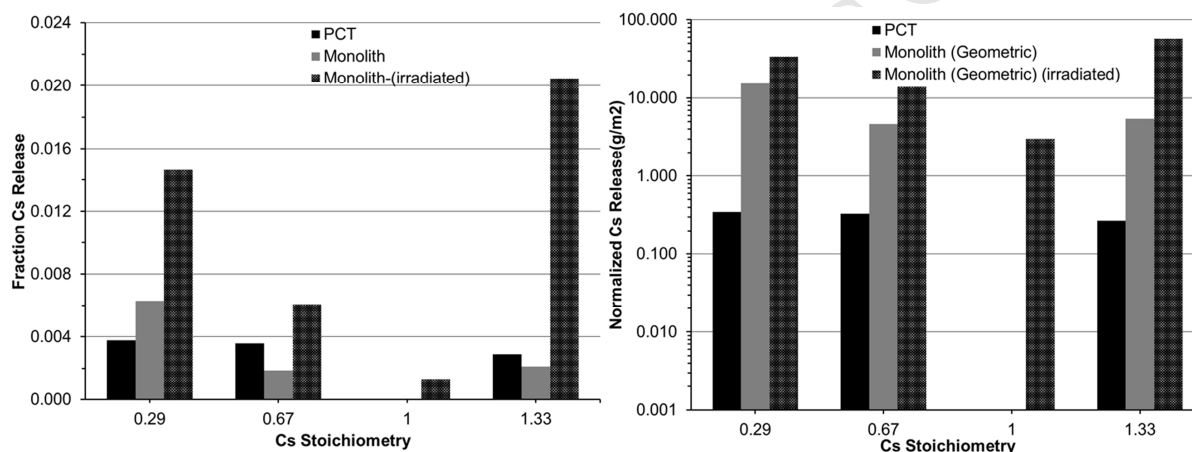


Figure 10. On the left, a), the fractional Cs release from the irradiated monolith samples is compared to the PCT and monolith results before irradiation. On the right, b), The normalized Cs release from monolith samples after irradiation was normalized by geometric surface area. The results are compared to PCT monolith leaching before irradiation

Surface area Brunauer–Emmett–Teller measurements of Cs029, Cs100 and Cs133 have shown that the surface area was several hundred times greater than measured by the geometric measurement. Additionally, Cs133 had twice the surface area of Cs029 but four times the fractional release indicating that surface area is not the sole cause for the increase in elemental loss. Overall these results indicate that radiation damage has a negative effect on hollandite stability noted by the doubling of its elemental leaching.

Leaching stability for hollandite also shows diminishing returns at high Cs content with minimum leaching near Cs = 1.00. The Cs release from Cs133 after irradiation was higher than the intermediate compositions though the Zn release was lower. This was probably due to Cs being released from the amorphized tunnel while Zn stays trapped in the octahedra. Also with no Ba in the Cs133 composition Cs diffusion would not be inhibited by the lower water affinity of Ba. Though this hypothesis is preliminary

it does explain the inconsistent leaching trend in light of the results and composition. While the mechanism for leaching has not been fully defined the relationship between Cs content, energetic stability, and elemental dissolution is apparent and can be used to develop more leach resistant hollandite waste forms. The optimal Cs content for leaching stability was found to be Cs=1.00.

Conclusion

A series of hollandite compositions across a full range of Cs substitutions, $0.00 \leq Cs \leq 1.33$, were irradiated with 1MeV Kr²⁺ ions to full amorphization and with 400 keV Kr²⁺ ions up to 1×10^{14} and 5×10^{14} Kr/cm². All experiments showed that radiation tolerance could be increased by Cs doping. The *in situ* tests revealed that as Cs content increased the critical dose for full amorphization increased while the change in amorphization onset was negligible. Additionally, the critical amorphization temperature of hollandite was found to be between 200 °C and 300 °C and decreased with increasing Cs content. The *ex situ* GIXRD and TEM cross-section images showed a distinct separation between the fully amorphous and crystalline zones.

Elemental leaching of hollandite showed that irradiated samples had twice the fractional Cs release compared to pristine samples. These results also show that Cs retention can be improved by increasing the Cs content as evidenced by the decreasing the amount of Cs released during leaching. However, at high Cs content the leaching stability suffers diminishing returns and shows that leaching is at a minimum for the Ba_{0.333}Cs_{1.000}Zn_{0.834}Ti_{7.166}O₁₆ composition. Leaching after irradiation resulted in increased Cs leach rates which was attributed to the damaged surface layer having inferior stability.

In summary, Cs incorporation had a stabilizing effect on the radiation tolerance and leaching behavior of hollandite. As such, hollandite wastefoms should be designed with higher Cs content to utilize the composition-dependent radiation and leaching stability.

Acknowledgments

KSB, RG and LSN acknowledge financial support from the DOE-EPSCoR Project Number: DE-SC0012530, "Radionuclide Waste Disposal: Development of Multi-scale Experimental and Modeling Capabilities." JA acknowledges the support of durability testing by the U.S. Department of Energy, Office of Nuclear Energy, Fuel Cycle Technology, Materials Recovery and Waste Form Development Campaign. Work conducted at Savannah River National Laboratory was supported by the U.S. Department of Energy under contract number DE-AC09-08SR22470. MT acknowledges the support of radiation damage study by the U.S. Department of Energy, Office of Nuclear Energy, Fuel Cycle Technology, Materials Recovery and Waste Form Development Campaign. Los Alamos National

Laboratory is operated by Los Alamos National Security, LLC, for the National Nuclear Security Administration of the US DOE under contract DE-AC52-06NA25396.

ACCEPTED MANUSCRIPT

Bibliography

- [1] V. Aubin-Chevaldonnet, D. Caurant, A. Dannoux, D. Gourier, T. Charpentier, L. Mazerolles, et al., Preparation and characterization of (Ba,Cs)(M,Ti)8O16 (M = Al³⁺, Fe³⁺, Ga³⁺, Cr³⁺, Sc³⁺, Mg²⁺) hollandite ceramics developed for radioactive cesium immobilization, *J. Nucl. Mater.* 366 (2007) 137–160. doi:10.1016/j.jnucmat.2006.12.051.
- [2] M.L. Carter, R.L. Withers, A universally applicable composite modulated structure approach to ordered BaxMyTi8-yO16 hollandite-type solid solutions, *J. Solid State Chem.* 178 (2005) 1903–1914. doi:10.1016/j.jssc.2005.03.040.
- [3] M. Tang, P. Tumurugoti, B. Clark, S.K. Sundaram, J. Amoroso, J. Marra, et al., Heavy ion irradiations on synthetic hollandite-type materials: Ba_{1.0}Cs_{0.3}A_{2.3}Ti_{5.7}O₁₆ (A=Cr, Fe, Al), *J. Solid State Chem.* 239 (2016) 58–63. doi:10.1016/j.jssc.2016.04.014.
- [4] R.C. Ewing, W.J. Weber, F.W. Clinard, Radiation effects in nuclear waste forms for high-level radioactive waste, *Prog. Nucl. Energy.* 29 (1995) 63–127. doi:10.1016/0149-1970(94)00016-Y.
- [5] A. Bystrom, A.M. Bystrom, The Crystal Structure of Hollandite, the Related manganese Oxide Minerals, and Alpha-MnO₂, *ACTA Crystallogr.* 3 (1950) 146–154. doi:10.1107/S0365110X5000032X.
- [6] A.E. Ringwood, S.E. Kesson, N.G. Ware, W. Hibberson, A. Major, The SYNROC process: A geochemical approach to nuclear waste immobilization, *Geochem. J.* 13 (1979) 141–165.
- [7] J. Amoroso, J.C. Marra, M. Tang, Y. Lin, F. Chen, D. Su, et al., Melt processed multiphase ceramic waste forms for nuclear waste immobilization, *J. Nucl. Mater.* 454 (2014) 12–21. doi:10.1016/j.jnucmat.2014.07.035.
- [8] E.R. Vance, G.R. Lumpkin, M.L. Carter, D.J. Cassidy, C.J. Ball, R.A. Day, et al., Incorporation of Uranium in Zirconolite (CaZrTi₂O₇), *J. Am. Ceram. Soc.* 85 (2004) 1853–1859. doi:10.1111/j.1151-2916.2002.tb00364.x.
- [9] S. Zlotnik, S.K. Sahu, A. Navrotsky, P.M. Vilarinho, Pyrochlore and Perovskite Potassium Tantalate: Enthalpies of Formation and Phase Transformation, *Chem. - A Eur. J.* 21 (2015) 5231–5237. doi:10.1002/chem.201405666.
- [10] R.L. Putnam, A. Navrotsky, B.F. Woodfield, J. Boerio-Goates, J.L. Shapiro, Thermodynamics of formation for zirconolite (CaZrTi₂O₇) from T=298.15 K to T=1500 K, *J. Chem. Thermodyn.* 31 (1999) 229–243. doi:10.1006/jcht.1998.0445.

- [11] R. Grote, M. Zhao, L. Shuller-Nickles, J. Amoroso, W. Gong, K. Lilova, et al., Compositional control of tunnel features in hollandite-based ceramics: structure and stability of $(\text{Ba,Cs})_{1.33}(\text{Zn,Ti})_8\text{O}_{16}$, *J. Mater. Sci.* (2018). doi:10.1007/s10853-018-2904-1.
- [12] K.S. Brinkman, R.K. Bordia, K.L. Reifsnider, W.K.S. Chiu, J. Amoroso, *A New Paradigm for Understanding Multiphase Ceramic Waste Form Performance*, 2014.
- [13] M.L. Carter, E.R. Vance, H. Li, Hollandite-rich Ceramic Melts for the Immobilisation of Cs, *MRS Proc.* 807 (2003) 249. doi:10.1557/PROC-807-249.
- [14] M.L. Carter, E.R. Vance, HIPed Tailored Ceramic Waste Forms for the Immobilisation of Cs, Sr and Tc, *MRS Proc.* 1107 (2008). doi:10.1557/PROC-1107-323.
- [15] B.M. Clark, P. Tumurgoti, S.K. Sundaram, J.W. Amoroso, J.C. Marra, V. Shutthanandan, et al., Radiation damage of hollandite in multiphase ceramic waste forms, *J. Nucl. Mater.* 494 (2017) 61–66. doi:10.1016/j.jnucmat.2017.07.013.
- [16] A. Abdelouas, S. Utsunomiya, T. Suzuki, B. Grambow, T. Advocat, F. Bart, et al., Effects of ionizing radiation on the hollandite structure-type: $\text{Ba}_{0.85}\text{Cs}_{0.26}\text{Al}_{1.35}\text{Fe}_{0.77}\text{Ti}_{5.90}\text{O}_{16}$, *Am. Mineral.* 93 (2008) 241–247. doi:10.2138/am.2008.2563.
- [17] V. Aubin-Chevaldonnet, D. Gourier, D. Caurant, S. Esnouf, T. Charpentier, J.M. Costantini, Paramagnetic defects induced by electron irradiation in barium hollandite ceramics for caesium storage., *J. Phys. Condens. Matter.* 18 (2006) 4007–4027. doi:10.1088/0953-8984/18/16/009.
- [18] J.L. Woolfrey, K.D. Reeve, D.J. Cassidy, Accelerated irradiation testing of SYNROC and its constituent minerals using fast neutrons, *J. Nucl. Mater.* 108–109 (1982) 739–747. doi:10.1016/0022-3115(82)90548-7.
- [19] K.A. Gowda, *Heavy Ion Bombardment of Zircon, Monazite and Other Crystal Structures*, 1982.
- [20] W.J. Weber, Effects of Alpha Irradiation on Barium Hollandite and Nickel-Iron Spinel, in: *Sci. Basis Nucl. Waste Manag. VIII. Held as Part Fall Meet. Mater. Res.*, 1985: pp. 671–678.
- [21] K.D. Reeve, J.L. Woolfrey, Accelerated Irradiation Testing of Synroc Using Fast Neutrons I. First Results on Barium Hollandite, Perovskite and Undoped Synroc B, *J. Am. Dent. Assoc.* 86 (1980) 10–14.
- [22] M. Tang, A. Kossoy, G. Jarvinen, J. Crum, L. Turo, B. Riley, et al., Radiation stability test on multiphase glass ceramic and crystalline ceramic waste forms, *Nucl. Instruments Methods Phys.*

- Res. Sect. B Beam Interact. with Mater. Atoms. 326 (2014) 293–297.
doi:10.1016/j.nimb.2013.10.092.
- [23] R.C. Ewing, L.M. Wang, Amorphization of zirconolite: alpha-decay event damage versus krypton ion irradiation, Nucl. Inst. Methods Phys. Res. B. 65 (1992) 319–323.
- [24] W.J. Weber, Effects of Alpha Irradiation on Barium Hollandite and Nickel-Iron Spinel, MRS Proc. 44 (1984) 671. doi:10.1557/PROC-44-671.
- [25] W.J. Weber, J.W. Wald, H.J. Matzke, Self-radiation damage in actinide host phases of nuclear waste forms, (1984) 681–686.
- [26] S.X. Wang, L.M. Wang, R.C. Ewing, Irradiation-induced amorphization: Effects of temperature, ion mass, cascade size, and dose rate, Phys. Rev. B. 63 (2000) 024105.
doi:10.1103/PhysRevB.63.024105.
- [27] W.J. Weber, Models and mechanisms of irradiation-induced amorphization in ceramics, Nucl. Instruments Methods Phys. Res. Sect. B Beam Interact. with Mater. Atoms. 166 (2000) 98–106.
doi:10.1016/S0168-583X(99)00643-6.
- [28] V. Aubin-Chevaldonnet, D. Gourier, D. Caurant, J.-M. Costantini, Transformation and clustering of defects induced by electron irradiation in barium hollandite ceramics for radioactive cesium storage: Electron paramagnetic resonance study, J. Appl. Phys. 111 (2012) 083504.
doi:10.1063/1.3702892.
- [29] S.E. Kesson, T.J. White, $[\text{Ba}_x\text{Cs}_y] [(\text{Ti},\text{Al})_{2x+y}\text{Ti}_{8-2x-y}] \text{O}_{16}$ Synroc-Type Hollandites II. Structural Chemistry, Proc. R. Soc. A Math. Phys. Eng. Sci. 408 (1986) 295–319.
doi:10.1098/rspa.1986.0122.
- [30] W.J. Weber, R.C. Ewing, L.-M. Wang, The radiation-induced crystalline-to-amorphous transition in zircon, J. Mater. Res. 9 (1994) 688–698. doi:10.1557/JMR.1994.0688.
- [31] K.E. Sickafus, R.W. Grimes, J.A. Valdez, A. Cleave, M. Tang, M. Ishimaru, et al., Radiation-induced amorphization resistance and radiation tolerance in structurally related oxides, Nat. Mater. 6 (2007) 217–223. doi:10.1038/nmat1842.
- [32] K.E. Sickafus, L. Minervini, R.W. Grimes, J.A. Valdez, M. Ishimaru, F. Li, et al., Radiation Tolerance of Complex Oxides, Science (80-.). 289 (2000) 748–751.
doi:10.1126/science.289.5480.748.

- [33] R.W. Cheary, R. Squadrito, Electron and X-ray diffraction from antiphase domains in the barium magnesium hollandite $Ba_{1.33}Mg_{1.33}Ti_{6.67}O_{16}$, *Acta Crystallogr. Sect. A Found. Crystallogr.* 48 (1992) 15–27. doi:10.1107/S0108767391008668.
- [34] M.C. Cadée, A. Prodan, Tripling of the short axis in the hollandite structure, *Mater. Res. Bull.* 14 (1979) 613–618. doi:10.1016/0025-5408(79)90043-6.
- [35] G. Bayer, W. Hoffman, Complex Alkali Titanium Oxides $A_x(B_yTi_{8-y})O_{16}$ of the α - MnO_2 Structure-Type, *Am. Mineral.* 51 (1966) 511–516.
- [36] J. Zhang, C.W. Burnham, Hollandite-type phases: Geometric consideration of unit-cell size and symmetry, *Am. Mineral.* 79 (1994) 168–174.
- [37] D.S. Filimonov, Z.K. Liu, C. a. Randall, An oxygen nonstoichiometry study of barium polytitanates with hollandite structure, *Mater. Res. Bull.* 37 (2002) 2373–2382. doi:10.1016/S0025-5408(02)00853-X.
- [38] N.E. Bibler, C.M. Jantzen, The Product Consistency Test and its Role in the Waste Acceptance Process for DWPF Glass, *Manag. Radioact. Wastes , Non-Radioactive Wastes from Nucl. Facil.* (1989) 743–749.
- [39] L.L. Hench, D.E. Clark, J. Campbell, High level waste immobilization forms, *Nucl. Chem. Waste Manag.* 5 (1984) 149–173. doi:10.1016/0191-815X(84)90045-7.
- [40] K.S. Brinkman, R.K. Bordia, K.L. Reifsnider, W.K.S. Chiu, J. Amoroso, *A New Paradigm for Understanding Multiphase Ceramic Waste Form Performance*, 2014.
- [41] K. Zhang, S. He, D. Yin, L. Peng, J. Wu, Self-propagating synthesis and aqueous durability of Nd-bearing zirconolite-rich composites using $Ca(NO_3)_2$ as the oxidant, *J. Nucl. Mater.* 478 (2016) 315–321. doi:10.1016/j.jnucmat.2016.06.033.
- [42] F. Angeli, P. McGlenn, P. Frugier, Chemical durability of hollandite ceramic for conditioning cesium, *J. Nucl. Mater.* 380 (2008) 59–69. doi:10.1016/j.jnucmat.2008.07.003.
- [43] D.R. F. Bart, H. Rabiller, G. leturcq, Leaching behavior of hollandite ceramics for cesium immobilization, *Atalante.* (2004) 1–4.
- [44] C.S. Dandeneau, T. Hong, K.S. Brinkman, E.R. Vance, J.W. Amoroso, Comparison of structure , morphology , and leach characteristics of multi-phase ceramics produced via melt processing and hot isostatic pressing, *J. Nucl. Mater.* 502 (2018) 113–122. doi:10.1016/j.jnucmat.2018.02.006.

- [45] T. Suzuki-Muresan, J. Vandenborre, A. Abdelouas, B. Grambow, S. Utsunomiya, Studies of (Cs,Ba)-hollandite dissolution under gamma irradiation at 95 ° C and at pH 2.5, 4.4 and 8.6, *J. Nucl. Mater.* 419 (2011) 281–290. doi:10.1016/j.jnucmat.2011.09.001.
- [46] Y. Xu, Y. Wen, R. Grote, J. Amoroso, L. Shuller Nickles, K.S. Brinkman, A-site compositional effects in Ga-doped hollandite materials of the form $Ba_xCs_yGa_{2x+y}Ti_{8-2x-y}O_{16}$: implications for Cs immobilization in crystalline ceramic waste forms, *Sci. Rep.* 6 (2016) 27412. doi:10.1038/srep27412.
- [47] Y. Xu, M. Feygenson, K. Page, L.S. Nickles, K.S. Brinkman, Structural Evolution in Hollandite Solid Solutions Across the A-Site Compositional Range from $Ba_{1.33}Ga_{2.66}Ti_{5.34}O_{16}$ to $Cs_{1.33}Ga_{1.33}Ti_{6.67}O_{16}$, *J. Am. Ceram. Soc.* 99 (2016) 4100–4106. doi:10.1111/jace.14443.
- [48] Y. Xu, R. Grote, Y. Wen, L. Shuller-Nckles, K.S. Brinkman, Development of Ga Doped Hollandites $Ba_xCs_y(Ga_{2x+y}Ti_{8-2x-y})O_6$ for Cs Immobilization, in: *Ceram. Energy Conversion, Storage, Distrib. Syst.*, John Wiley & Sons, Inc., Hoboken, NJ, USA, 2016: pp. 157–164. doi:10.1002/9781119234531.ch14.
- [49] J.F. Ziegler, M.D. Ziegler, and J.P. Biersack, “SRIM – The stopping and range of ions in matter (2010),” *Nucl. Inst. Methods Phys. Res. B*, 268 [11–12] 1818–1823 (2010).
- [50] S. Gunaseelan, R. Rao, A. Manimaran, E. Ramu, and B. Sivakumar, “Determination of traces of amorphous cefuroxime axetil content in cefuroxime axetil crystalline drug substance using modulated differential scanning calorimetry (MDSC),” *J. Chem. Pharm. Res.*, 4 [11] 4743–4751 (2012).
- [51] Rigaku, Rigaku PDXL Software Manual, 1–59 (2012).
- [52] C. Jiang, K.J. McClellan, Y.-Q. Wang, D.D. Byler, M.K. Patel, I.O. Usov, et al., Role of Antisite Disorder on Preamorphization Swelling in Titanate Pyrochlores, *Phys. Rev. Lett.* 108 (2012) 1–5. doi:10.1103/physrevlett.108.195504.
- [53] ASTM and C1220-10, “Standard Test Method for Static Leaching of Monolithic Waste Forms for Disposal of Radioactive Waste,” 14 [December] (2010).
- [54] T. Murakami, B.C. Chakoumakos, R.C. Ewing, G.R. Lumpkin, W.J. Weber, Alpha-decay event damage in zircon, *Am. Mineral.* 76 (1991) 1510–1532.
- [55] M.L. Carter, Tetragonal to monoclinic phase transformation at room temperature in $Ba_xFe_{2x}Ti_{8-2x}O_{16}$ hollandite due to increased Ba occupancy, *Mater. Res. Bull.* 39 (2004) 1075–1081.

doi:10.1016/j.materresbull.2004.02.018.

- [56] M. Tang, P. Lu, K. Sickafus, RADIATION DAMAGE EFFECTS IN RARE EARTH SESQUIOXIDES UNDER ION IRRADIATION, (2006).

ACCEPTED MANUSCRIPT

Supplementary

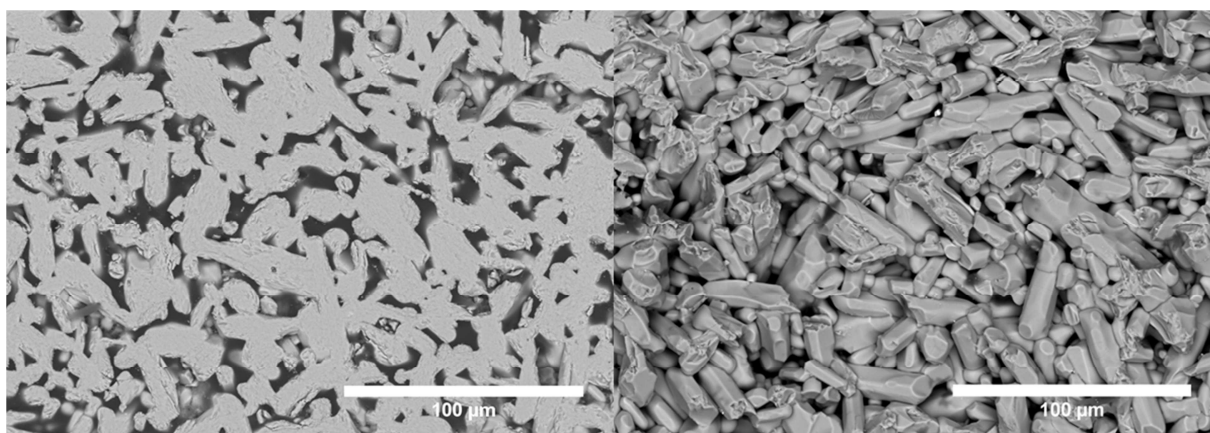


Figure S1: SEM of polished hollandite Cs067-2 before irradiation (left) and after irradiation (right)

- Cesium incorporation increased hollandite's radiation and leaching stability
- Critical dose for amorphization doubled after full cesium substitution
- Critical amorphization temperature for hollandite was between 200-300°C
- Irradiation doubled fractional cesium released during leaching

ACCEPTED MANUSCRIPT